Contents lists available at ScienceDirect

International Journal of Impact Engineering

Head-on impact of metal microparticles: Aggregation or separation?

Jianqiao Hu [a,b], Xiaoming Liu [a,b,*], Yueguang Wei [c]

[a] *LNM, Institute of Mechanics, Chinese Academy of Sciences, Beijing 100190, PR China*
[b] *School of Engineering Science, University of Chinese Academy of Sciences, Beijing 100049, PR China*
[c] *Department of Mechanics and Engineering Science, College of Engineering, Peking University, Beijing 100871, PR China*

ARTICLE INFO

ABSTRACT

During the head-on particle collision, the adhesion plays a more important role as theparticle size decreases to micro size; the increasing surface effect makes the particle prefer to aggregate. While on the other hand, as the impact velocity increases, particles prefer to separate because of the larger elastic repulsive interaction. Another factor, which cannot be ignored during the impact of metal microparticles, is the dislocation plasticity which shows the rate and size effect. In this work, taking nano-plasticity behavior into account, our molecular simulations revealed two critical impact velocities for the transition of particle collision from separation to aggregation, and these two velocities are quantified by the analytical models proposed in this study. The low critical velocity for particle aggregation is dominated by adhesion, while in contrast, the high critical velocity for aggregation is dominated by dislocation plasticity, where the dislocation density in the particle after the collision is proportional to the impact velocity. With these findings, an analytical model was proposed to determine the critical particle size, below which no separation will be found whatever the impact velocity is. And this critical size is proportional to the ratio of surface energy to stacking fault energy.

1. Introduction

Particle collision is ubiquitous in natural phenomena as well as in engineering applications, such as the transportation of sand and powder, collection of dust particles [1,2], the technical sprays in manufacturing processes [3], and the programmable particles patterning [4]. During the collision of particles, the interaction force has three parts: elastic rebound, dissipation due to viscous deformation, and adhesion caused by molecular forces [5]. The interplay between these three parts leads to two endings of particle collision, i.e., the restitutive collisions where particles separate after the collision and the aggregative collisions where particles constitute a joint aggregate. Understanding the fundamental mechanisms associated with the patterns of particle collisions can facilitate the regulation of particle morphology and kinematics [6].

For the particle separation after a collision, the restitution coefficient, defined by the ratio of the normal rebound velocity to the normal impact velocity, is used to quantify the collisions. Previous studies showed that the restitution coefficient as well as the failure of the colliding particles depends on not only the impact angle and velocity [7, 8], but also the material properties such as adhesion and plasticity [9, 10]. Increasing adhesion between the colliding particles leads to a

higher critical velocity below which the particles aggregate after the collision [5]. Besides the impact velocity and material property, particle size also plays a vital role in collisions, which was studied in experiments [11,12] and numerical simulations [13,14]. As the particle size decreases to nano-scale, in addition to the size effect of plasticity [15,16], the effect of adhesion between the particles becomes prominent, making the colliding particles prefer to aggregate [17].

Previous studies [18,19] revealed that whether the particles aggregate or separate after the collision depends on the particle plasticity and adhesion. Based on the quasi-static contact mechanics, Thornton and Ning [20] developed an analytical model to determine the critical velocity for the transition from the aggregation to the separation of adhesive elastic particles; however, due to the assumption in the model that the deformation is elastic, the critical velocity only highlights the adhesion effect. Subsequently, considering the particle plasticity by assuming a constant hardness, Weir and Mcgavin [21] derived the critical velocity which identifies a low limit above which the particles separate after the collision; in this model, the critical velocity is proportional to the surface energy and inversely proportional to $\sqrt{Y}$ with Y being the particle hardness. These analytical studies help gain insight into the effects of particle plasticity and adhesion on particle collisions.

Table 1

Simulation parameters for the collision of particles with coarse-grained potentials.

Parameters	Values
Particle radius (r_0)	10~100
Number of atoms	11,844~11,847,076
Impact velocity r_0 / t_0)	0.05~2.5
Time step (t_0)	0.0025
Temperature (ε / k_B)	0.005
Adhesion ratio, λ	0~2.5

However, the above models of particle collisions are developed based on the theory of quasi-static continuum mechanics, while it was found that the impact of nanoparticles shows a strong size effect on the colliding plasticity [22]. Therefore, the above analytical models remain unclear for the collisions of nanoparticles when the size effect is prominent. What is more, for the particle collisions with high impact velocities [23], shock-induced plasticity exists in particles, featuring high contact pressure and large deformation of particles. In this case, the particles prefer to aggregate [24] due to the large amount of energy dissipated by plastic deformation; as a result, the restitution coefficient approaches zero [25]. These studies indicate that in addition to the low critical velocity where the quasi-static contact mechanics holds [26], there exists an upper limit of high impact velocity above which the particles would aggregate again. However, most studies for particle collisions at the high impact velocity hover around the patterns of particle failure [27,28], and the quantitative understanding of the upper critical velocity is still missing. In this study, we try to quantify the two critical velocities for the transition of particle collisions from aggregation to separation, and clarifying this issue will help regulate particle collisions in engineering applications.

In this paper, in order to address the issues when and how the particles aggregate or separate after a collision, we studied the head-on collisions of particles by molecular dynamics (MD) simulations using a series of modified coarse-grained potentials [29]. Also, we developed analytical models to predict two critical impact velocities for the transition of particle collisions from separation to aggregation and further determined a critical size below which the particles always aggregate. Moreover, we performed MD simulations with two metallic particles, i. e., copper and tungsten, to verify the critical size predicted by the analytical models. The paper is organized as follows:Section 2 describes the MD modeling details for the particle collisions. Section 3 introduces the analytical models and presents the simulation results for the collisions of particles with the coarse-grained potentials. Section 4 further discusses the collisions of metallic particles, i.e., tungsten and copper.

Finally, Section 5 summarizes our findings.

2. Methodology and model description

In this study, the particle collision is performed by using the Large-scale Atomic/Molecular Massively Parallel Simulator [30], with parameters in Table 1. As illustrated in Fig. 1, the head-on collision model consists of two spherical particles of the same radius, and the particle radius R ranges from $10r_0$ to $100r_0$ (r_0 is a reduced length unit and corresponds to the equilibrium bond length between atoms). Correspondingly, the total number of atoms is from 11,844 to 11,847,076. The atoms in the two particles are all located in a perfect face-centered cubic (FCC) crystalline structure with crystal orientations being x-[100], y-[010] and z-[001], respectively.

In order to get a universal law for the impact of adhesive particles, we used the modified coarse-grained potentials [29] (see Appendix A) instead of the real potential to describe the interaction between atoms in the particles. Compared to the real potential, the modified coarse-grained potentials have the advantages that the material properties such as the particle ductility or the adhesion between the particles can be tuned individually without changing the elastic properties. Therefore, to understand the effects of plasticity and adhesion, we tuned the particle properties in two folds: first is the particle ductility, which is modified by changing the potential tail; second, the interfacial adhesion between particles is changed by an adhesion ratio λ, where a larger value of λ denotes a stronger interfacial adhesion. In the simulation, the two particles are deformable with the same material property. The interaction potential between the particles, if not explicitly stated, is the same as the one used within the particle.

In the simulations, non-periodic boundary conditions are applied in three directions, i.e., x, y, and z directions. Before the collision, the two particles are first energy minimized to relax their structure and then equilibrated to a target temperature of $0.005\varepsilon/k_B$ for $50t_0$ (k_B is the Boltzmann constant, and t_0 is the reduced time unit) with a time step of $0.0025t_0$. The simulations with another two time steps, i.e., $0.001t_0$ and $0.004t_0$ are also performed, and this alters the results only negligibly. Subsequently, the head-on collision of particles is imposed along the x direction. The particle on the left has an initial velocity of v_x ranging from $0.05r_0/t_0$ to $2.5r_0/t_0$ with an increment of $0.05r_0/t_0$ for each simulation, and the right particle is initially fixed. During the collision, we recorded the positions and velocities of the center-of-mass for the two particles and obtained the restitution coefficient as the ratio of the rebound velocity to the impact velocity. For each impact velocity, whether the particles aggregate or separate after a collision is determined by analyzing the patterns of particle motion, including the
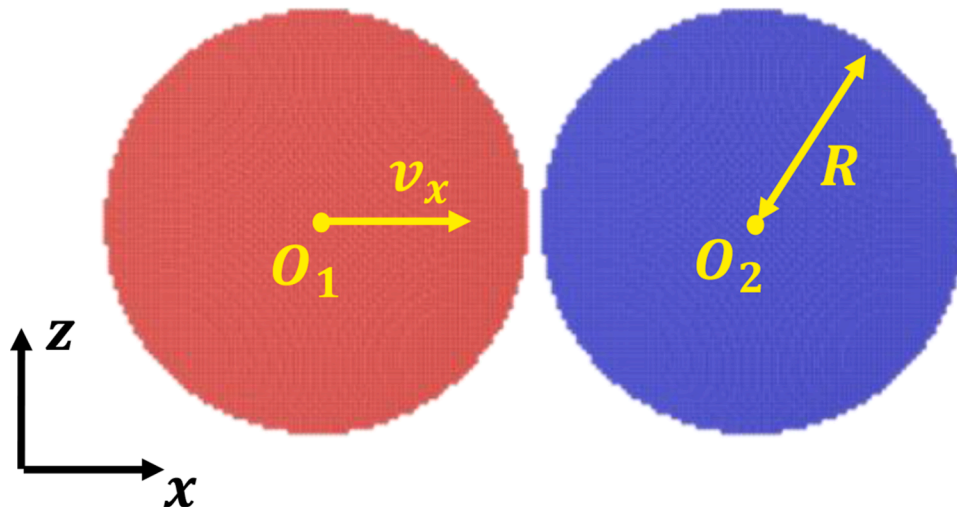

Fig. 1. Geometrical model of particle collision. The two particles are colored differently for the analysis of particle motion.
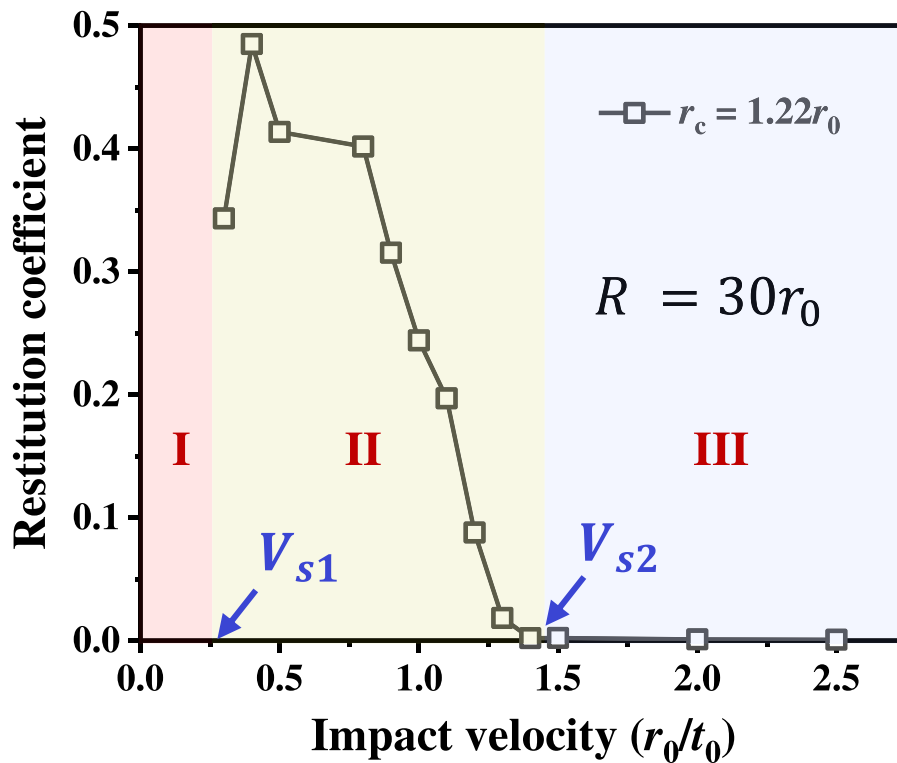
Fig. 2. Three collision regimes divided by two critical impact velocities; $V_{s1} = \sim 0.25 r_0/t_0$ and $V_{s2} = \sim 1.5 r_0/t_0$. Regime I: aggregation; Regime II: separation; Regime III: aggregation.
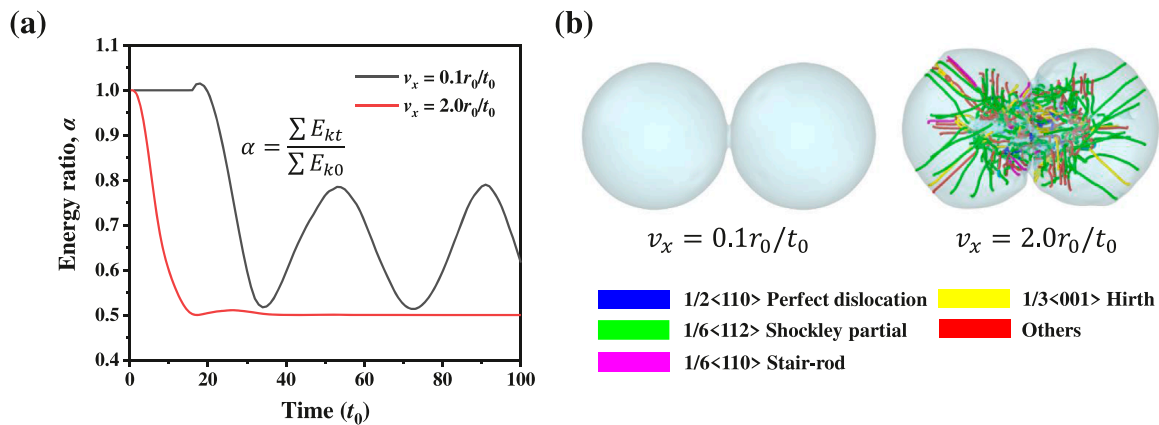

Fig. 3. (a) Evolution of energy ratio and (b) dislocation structures after impact with two collision velocities.

positions and velocities of two particles. Deformation of particles can be denoted by $\delta/2R$, where δ is defined by $\delta = 2R - l$ and l is the distance between the center-of-mass of two particles.

To obtain the dislocation density, we first used the dislocation extraction algorithm (DXA) [31] method to track dislocations and obtained the total length of dislocations in the two colliding particles; the dislocation density is then evaluated by dividing the dislocation length by the total volume of undeformed particles. In addition, the dislocation structures and atomic deformation were visualized by the open-source software OVITO [32].

3. Aggregation and separation of particles

In this section, we studied when and how the particles aggregate or separate after the collisions by analyzing the particle motion, the dislocation structures, and the kinetic energy of the particles. Also, we

developed analytical models to determine two critical velocities for the transition of particle collisions from aggregation to separation.

3.1. Two critical velocities for particle aggregation

To study when the particles aggregate or separate after the collisions, we simulated the head-on impact of particles ($r_c = 1.22 r_0$) with a radius of $30 r_0$ over a wide range of impact velocities. As the velocity increases, the colliding particles first aggregate at the low velocities, separate within a certain range of velocities, and aggregate again at the high velocities. The three regimes are separated by two critical velocities, i.e., V_{s1} and V_{s2}, as shown in Fig. 2.

For regime I, below the impact velocity of V_{s1}, the particles aggregate and vibrate around the center-of-mass of the system. For regime II between the two critical velocities, the particles separate after the collision because the elastic rebound overcomes the adhesion. In addition, there
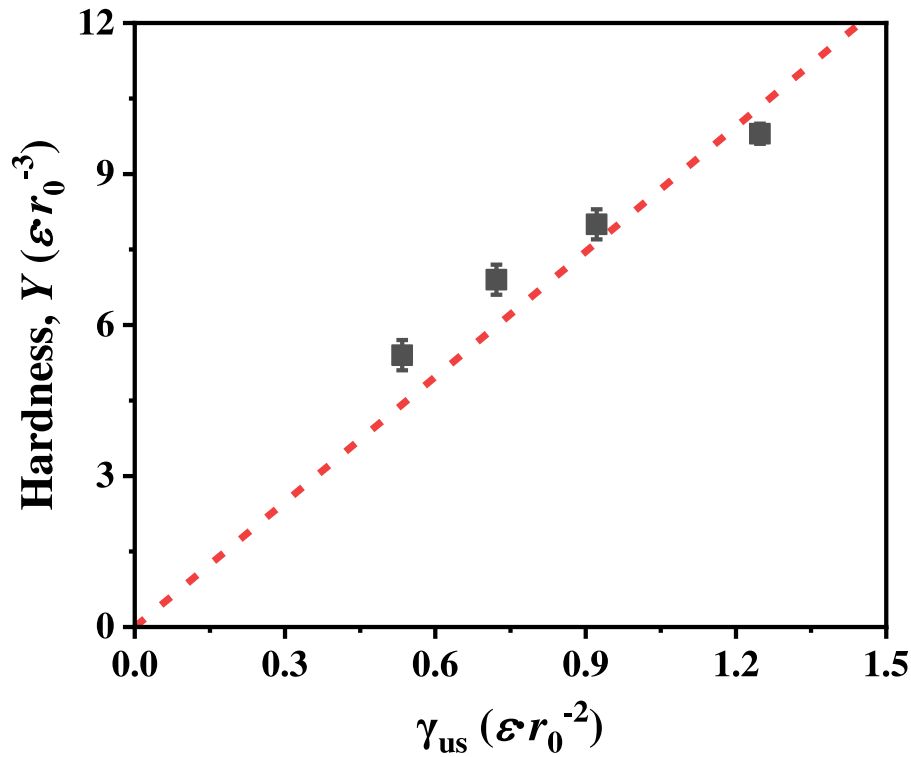
Fig. 4. Linear relation between unstable stacking fault energy and hardness for materials with modified Morse potentials.

exists a peak restitution coefficient at the impact velocity of $\sim 0.4 r_0 / t_0$. This peak is consistent with the previous study in [33] and can be interpreted by the balance of competition between the repulsive interaction and the cohesive interaction between particles. For regime III beyond the critical velocity of V_{s2}, the particles aggregate, and the restitution coefficient is around zero. The restitution coefficient of zero indicates that the particle deformation dissipated most of the energy with little elastic recovery. This finding is consistent with the experimental observation [34] that the aluminum microparticles rebound from the aluminum substrates at moderate impact velocities but bond to the substrates when the impact velocity is extremely high, and in the case of high-velocity impact, the restitution coefficient approaches zero due to the bonding of particles. Corresponding to the three regimes in Fig. 2, the videos for the evolution of particle patterns are provided as supplementary materials.

By further analyzing the kinetic energy and the dislocation structures during the collision, we found that the particle aggregation at low and high impact velocities (Regimes I and III) can be attributed to different mechanisms. In regime I, the particles remain aggregation because the repulsive force caused by elastic rebound is smaller than the adhesion force, whereas in regime III, there is little elastic recovery and a large number of dislocation plasticity leads to the particle yielding. Here, we introduced an energy ratio α by dividing the kinetic energy by the initial kinetic energy, as shown in Fig. 3(a). For a lower impact velocity of $0.1 r_0 / t_0$ in regime I, the particle deformation is almost elastic with few dislocations during the collision (see Fig. 3(b)); in this situation, the two particles stick together, and the kinetic energy fluctuates with time. Notably, the peak of energy ratio is less than 1.0 after the collision, and this indicates that the dissipation of kinetic energy occurs in the initial collision of nanoparticles due to the contact dynamics [13]. For a higher impact velocity of $2.0 r_0 / t_0$ in regime III, numerous dislocations nucleated in the particles, as shown in Fig. 3(b). A large amount of dislocation plasticity leads to energy dissipation, and thus the particles yield with little elastic recovery. As a result, the energy ratio finally drops to ~ 0.5 (see Fig. 3(a)).

3.2. Classical model for the low critical velocity

For the low critical velocity of V_{s1}, the analytical model was developed based on the quasi-static contact mechanics because only limited dislocation plasticity exists at this impact velocity. By assuming a constant hardness Y of a particle during the collision between the particle and a rigid plane, Weir and McGavin [21] derived the critical velocity beyond which the particle separates from the plane due to the elastic rebound. The formula is given by

$$V_{s1} = k_0 \left(\frac{\gamma_s^2}{\rho Y R^2} \right)^{1/2}. \tag{1}$$

Here, k_0 is a parameter of ~ 0.74, γ_s is the surface energy between the particle and the plane, ρ is the mass density of the particle, Y is the particle hardness, and R is the particle radius. For the above collision model, the formula of V_{s1} was also written in forms with different parameters of k_0 [20,35]. However, the basic relation remains valid that the critical velocity is proportional to the surface energy and inverse to the particle size.

Particularly, Rice [36] revealed that the critical resolved shear stress is proportional to the unstable stacking fault energy γ_{us} when the dislocations dominate plasticity. Therefore, in this study, we assumed that the particle hardness in Eq. (1) is proportional to the unstable stacking fault energy and confirmed this linear relation in the particles characterized by the modified Morse potentials, as shown in Fig. 4. The hardness varies due to the change of cut-off radius in the modified Morse potentials, and the details for the calculation of particle hardness can be found in Appendix A. Then, by considering the linear relation between the particle hardness and the unstable stacking fault energy, we can rewrite Eq. (1) as

$$V_{s1} = k_1 \left(\frac{\gamma_s^2 b}{\rho \gamma_{us} R^{*2}} \right)^{1/2}, \tag{2}$$

where k_1 is a parameter, b is the magnitude of Burgers vector, and R^* is the equivalent radius based on Hertzian contact theory. In this study, for
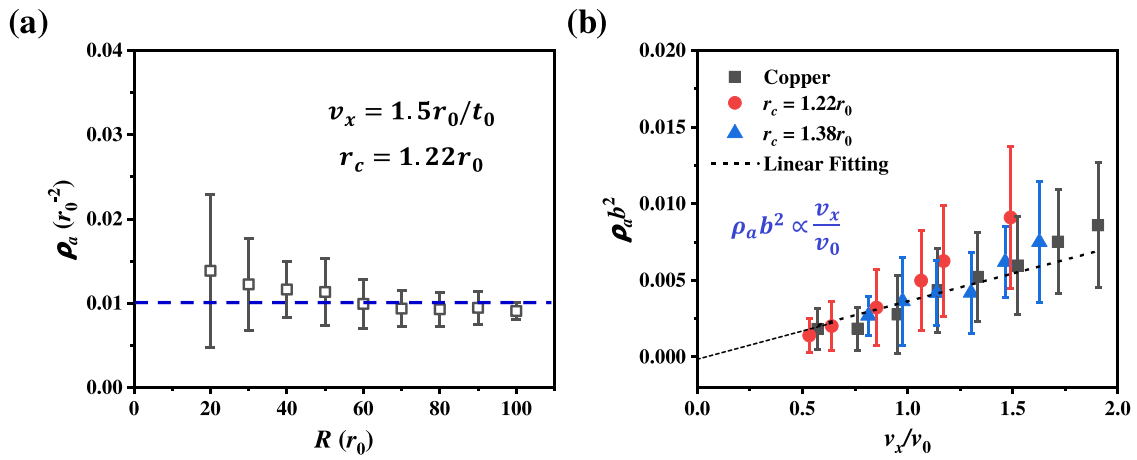
(a)

(b)

Fig. 5. (a) Equivalent dislocation density in particles of different sizes and (b) linear relation between dislocation density and impact velocity in particles of different materials. The gray shaded region corresponds to the 95% confidence band.
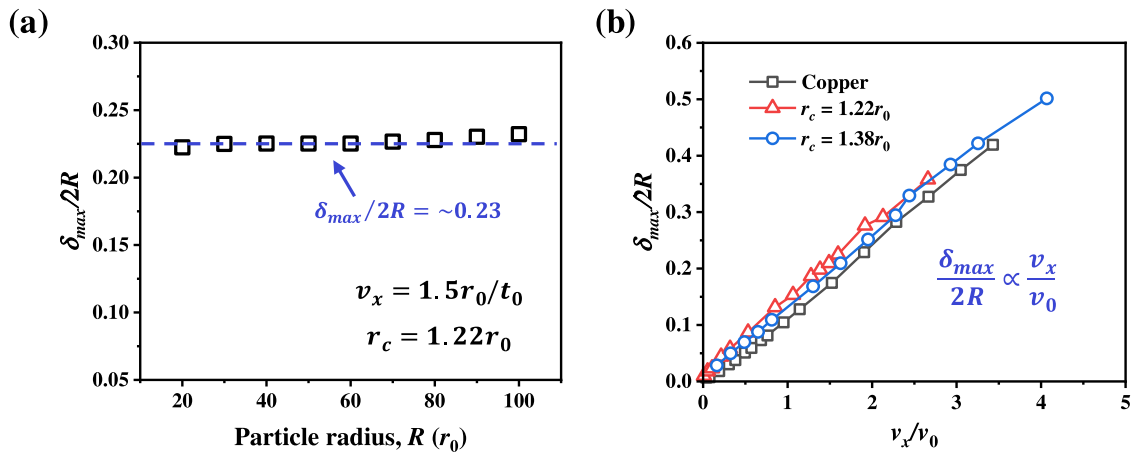
(a)

(b)

Fig. 6. The maximum deformation for (a) the particles of different sizes at the velocity of $1.5r_0/t_0$ and (b) the particles of different materials.
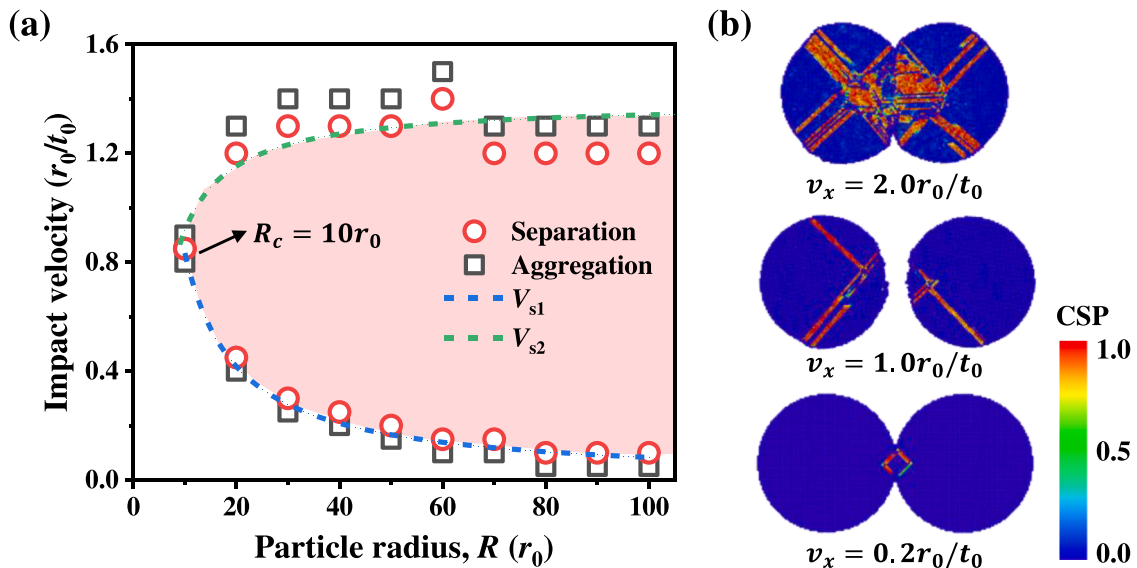
(a)

(b)

Fig. 7. (a) Two critical velocities for the collision of particles with $r_c = 1.22r_0$. The dash lines are obtained from the analytical model (the blue line corresponds to V_{s1} and the green line is V_{s2}), and the symbols are simulation results. The red shaded region corresponds to the particle separation predicted by the analytical models. (b) The final patterns of particle collisions at three impact velocities; the particle radius is $30r_0$ and the atoms are colored according to their central symmetry parameter (CSP) [39].
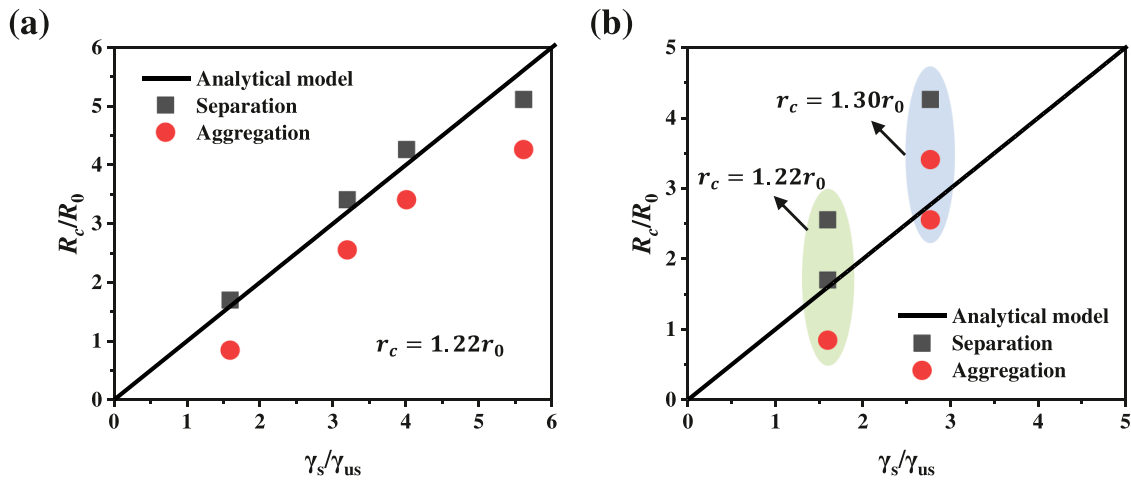
(a)

(b)

$r_c = 1.30r_0$

$r_c = 1.22r_0$

$r_c = 1.22r_0$

Fig. 8. Critical radius for particle aggregation as (a) the surface energy varies and (b) the unstable stacking fault energy varies.

Table 2
Materials properties for two kinds of particles.

Materials	γ_{us} (mJ /m^2)	γ_s on (001) Plane (mJ/m^2)	Lattice constant, a (nm)	Critical radius, R_c (nm)
Tungsten	1716	2930	0.314339	~3
Copper	158	1345	0.3613	~13

the collision of two particles of the same radius R, the equivalent radius is $R/2$.

3.3. New model for the high critical velocity

For the high critical velocity of V_{s2}, although previous studies [27, 28] were carried out to reveal the mechanisms of particle failure at high impact velocities, the quantitative analysis for the high critical velocity remains ambiguous. Based on the analyses in section 3.1, we can see that above the high critical velocity, the dislocation plasticity dissipates most of the elastic energy, resulting in the full inelastic collision with the restitution coefficient approaching zero. Here, we established an analytical model based on the energy balance; namely, the decrease of

(a)

(b) $v_x = 300$ m/s
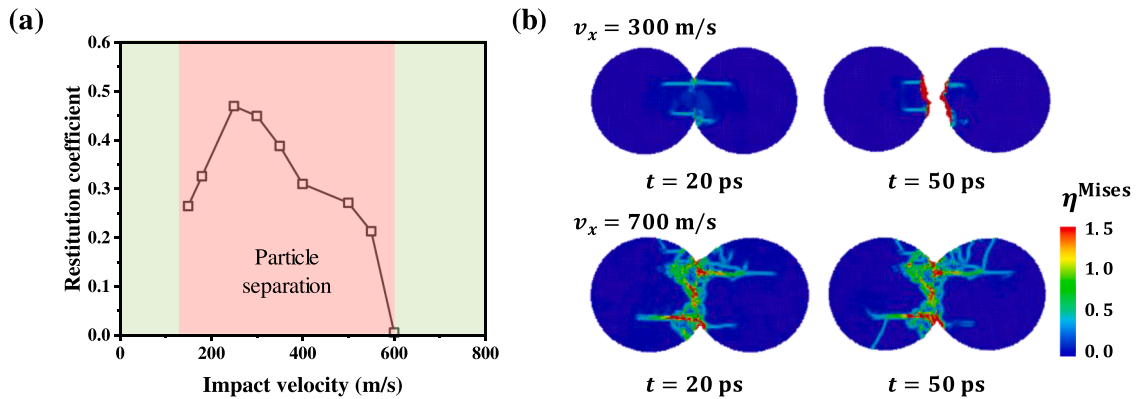
Fig. 9. (a) The restitution coefficient for tungsten particles at different impact velocities. Only the restitution coefficient for particle separation is shown. (b) Distribution of atomic equivalent strain when particles separate (300 m/s) or aggregate (700 m/s).
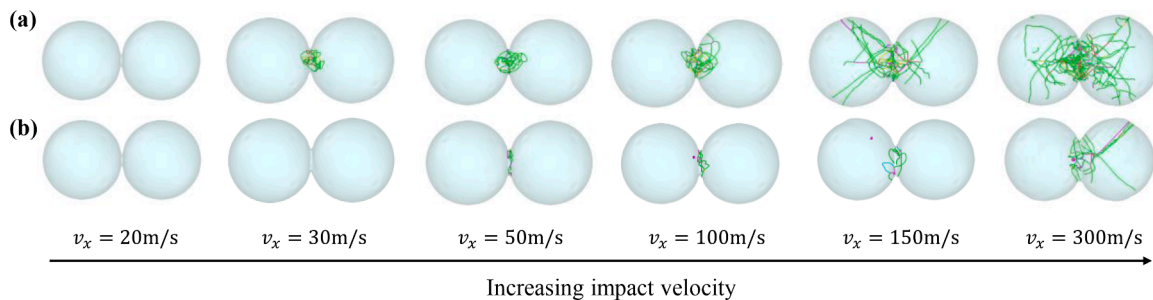

Fig. 10. Dislocation structures during the collision of copper particles at the time (a) when the number of dislocations are maximum and (b) when the dislocations remain stable finally.

the kinetic energy of the system is equal to the plastic dissipation of dislocations and the change of surface energy. The equation is given as follows.

$$\frac{1}{4}mV_{s2}^2 = \rho_a \cdot 2 \cdot \frac{4}{3}\pi R^3 \cdot k_{20}b \cdot \gamma_{us} - 2\gamma_s \pi r_c^2. \qquad (3)$$

Here, m is the particle mass, ρ_a is the equivalent dislocation density in a particle during the collision, $k_{20}b$ presents the distance of dislocation motion, and r_c is the critical contact radius during the collision.

Next, we quantified the plastic dissipation and the surface energy in Eq. (3) by analyzing the dislocation density and the contact deformation at high impact velocities. First, to determine the dislocation plasticity during the collision, we introduced the equivalent dislocation density ρ_a by averaging the maximum dislocation density ρ_m and the final stable dislocation density ρ_s during the collision and used the standard deviation of ρ_m and ρ_s to present the error bar. As shown in Fig. 5(a), the dislocation density ρ_a exhibits a weak size dependence at a high impact velocity. However, in Fig. 5(b), similar to the analysis of the particle deformation at high-speed impact [21], we normalized the impact velocity v_x by a characteristic velocity v_0 which is expressed as $\sqrt{\gamma_{us}/\rho b}$ and found a unified linear relation between dislocation density and the normalized impact velocity for the collisions of particles with different materials.

Second, in Eq. (3), the variation of surface energy is related to the area of contact surface during the collision. To obtain the maximum contact radius r_c during the head-on collision of particles, we calculated the maximum colliding deformation $\delta_{max}/2R$ because the contact radius r_c and the compressive displacement δ_{max} have a relation of $r_c^2 = \delta_{max}R$. As shown in Fig. 6, we found that the maximum deformation at high impact velocity exhibits weak size dependence and is proportional to the normalized velocity v_x/v_0 for colliding particles of different materials. This finding is consistent with the theoretical model in the collision between a particle and a rigid plane [21] that the normalized deformation δ_{max}/R of the particle linearly depends on the normalized impact velocity in the case of high impact velocity.

Considering the linear dependence of dislocation density and colliding deformation on impact velocity, we can further write Eq. (3) as

$$\frac{1}{4}mV_{s2}^2 = \frac{k_2}{b^2}\sqrt{\frac{\rho b}{\gamma_{us}}}V_{s2} \cdot 2 \cdot \frac{4}{3}\pi R^3 \cdot b \cdot \gamma_{us} - 2\gamma_s \pi k_3 \sqrt{\frac{\rho b}{\gamma_{us}}}V_{s2}R^2. \qquad (4)$$

Then, from Eq. (4), we can obtain the high critical velocity as

$$V_{s2} = 8k_2\sqrt{\frac{\gamma_{us}}{\rho b}} - \frac{6k_3\gamma_s}{\rho R}\sqrt{\frac{\rho b}{\gamma_{us}}}, \qquad (5)$$

where k_2 and k_3 are two parameters associated with the dislocation plasticity and the colliding deformation, respectively. The above formula of V_{s2} provides an insight into the particle aggregation or separation at high impact velocity. Besides the particle radius R, the analytical model of Eq.(5) also bridges the connection between the high critical velocity and the inherent material properties, such as the unstable stacking fault energy γ_{us} and the surface energy γ_s.

3.4. Size dependence of particle collision

From the analytical models of two critical velocities, we can see that as the particle radius increases, the lower critical velocity V_{s1} decreases, whereas the critical velocity V_{s2} increases. Next, we confirmed the size dependence of the two critical velocities in analytical models by simulating the collisions of particles with radii ranging from $10r_0$ to $100r_0$ at various impact velocities. For each particle size and impact velocity in the simulations, we can determine whether the particles aggregate or separate after a collision and thus obtain the critical velocity for the transition from particle separation to aggregation.

As shown in Fig. 7(a), the simulation results demonstrated the size

dependence of the two critical velocities, and the parameters in the analytical models for two critical velocities can be fitted from the simulation results, with non-dimensional parameters k_1, k_2, and k_3 being 2.77, 0.1848, and 0.5219, respectively. Also, the particle patterns after a collision are illustrated in Fig. 7(b) to present the transition between particle aggregation and separation as the impact velocities vary. Both analytical and simulation results in Fig. 7(a) indicated that the two critical velocities exhibit opposite dependences on the particle size. On the one hand, as the particle size increases, the critical velocity V_{s1} decreases. This size dependence is consistent with the experimental observation in the collisions of nanoparticles of silver and sodium chloride [35] that the critical velocity V_{s1} decreases with the increasing particle size. Also, our analytical predictions and simulation results of V_{s1} showed the same size dependence as the experimental results [35]. On the other hand, as the particle size increases, the critical velocity V_{s2} increases. Corresponding to the particle aggregation at high impact velocity [17,24], we found that the dislocation density exhibits a linear dependence on the impact velocity (see Fig. 5(b)) and analytically determined the high critical velocity V_{s2} in this study for the transition from the particle separation to aggregation. Coincidentally, prior impact experiments of copper microparticles [37] demonstrated that as the impact velocity increases and exceeds a critical value, the restitution coefficient decreases, and approaches zero due to the particle bonding. The analytical models for the above two critical velocities can be validated by the impact experiments of metal microparticles [37, 38]; whether the particles rebound from or bond to the substrates can be in-situ observed, and thus the critical velocity for the transition from the rebound to bonding can be obtained. Furthermore, as the particle radius decreases to $\sim 10r_0$, the two critical velocities are almost equal (see Fig. 7(a)). Below the critical radius of $10r_0$, the two particles would always aggregate after the collision.

Particularly, the low critical velocity of V_{s1} in this study was developed for the case of plastic collision. In Fig. 7(a), both analytical models and simulation results indicate that the critical velocity of V_{s1} decreases as the particle size increases. Therefore, due to the decrease of the velocity V_{s1} for the larger particles, the colliding deformation would become elastic. By analyzing the simulation results, we found that when the particle radius exceeds $\sim 80r_0$, the collision is elastic at the velocity of V_{s1}, characterized by the absence of dislocation nucleation. This finding is consistent with the experimental observation of the collisions of silver and sodium chloride particles [35], whose deformation becomes elastic at V_{s1} when particle radii increase to ~ 20 nm and ~ 10 nm, respectively. For the elastic impact, the analytical model for V_{s1} should be established based on the adhesive elastic collision which was discussed in [20].

3.5. Critical size for particle aggregation

By combining the analytical models of the two velocities in Eq. (2) and Eq. (5), we can further obtain a critical particle size below which the particles would always aggregate despite the change of impact velocities. The critical particle radius R_c is given by

$$R_c = \frac{\gamma_s}{\gamma_{us}}R_0. \qquad (6)$$

Here, R_0 is a characteristic length, and $R_0 = \frac{(k_1+3k_3)b}{4k_2}$. The above formula indicates the critical radius for the particle aggregation primarily depends on the ratio of surface energy and unstable stacking fault energy (γ_s/γ_{us}). For the model materials, the R_0 is $\sim 5.87b$ by using k_1, k_2, and k_3 obtained in Section 3.4.

For particle collisions in real engineering, the particle materials are various and thus have different unstable stacking fault energies; on the other hand, the adhesion between the particles also varies and is caused by surface and field forces, e.g., van der Waals, electrostatic and magnetic forces [19]. Subsequently, by individually regulating the surface

energy and the unstable stacking fault energy in the simulations of particle collisions, we verified the analytical model of the critical size in Eq.(6) from two aspects. First, to study the effect of surface energy, we modified the potential used between the two particles with $r_c = 1.22r_0$ by varying the potential well ε_0 with $\lambda \cdot \varepsilon_0$ (see Appendix A) to achieve different surface energies between particles. Compared to the original surface energy γ_s between the two particles, the surface energy is changed to $\lambda \cdot \gamma_s$ by the ratio λ. Through this modification, we changed the surface energy between particles and kept the unstable stacking fault energy of particles unchanged. Second, the particles are characterized by the model materials with potentials of different cut-off radii (see Appendix A). In this case, we modified the unstable stacking fault energy and kept the surface energy the same. Using the above modification of potentials and simulating the head-on collisions with a wide range of impact velocities, we determined whether the particles of a certain radius can always aggregate after the collision.

As shown in Fig. 8, we presented the analytical predictions of Eq. (6) and the simulation results for the relation between the critical radius and the γ_s/γ_{us}. For either the change of γ_s in Fig. 8(a) or the change of γ_{us} in Fig. 8(b), the analytical predictions are consistent with the simulation results over a wide range of γ_s/γ_{us}. For particles with increased surface energy, the particles tend to aggregate after the head-on collisions because more energy is required to separate the particles after the contact. Also, for particles with decreased stacking fault energy, the dislocation plasticity can be easily activated due to the low value of γ_{us} and then full dissipate the kinetic energy; thus the particles prefer to aggregate after the collision.

However, for a more ductile particle with $r_c = 1.38r_0$, the critical radius R_c predicted by the analytical model is $\sim 22r_0$, whereas in the simulations, we found that the particles remain aggregation as the particle radius increases to $35r_0$. This inconsistency between the analytical and simulation results is attributed to the fact that the energy dissipated by the viscoplasticity [40] and the colliding fluctuation [41] cannot be ignored for the particles with more ductility.

4. Particle collision for metal

In section 3, analytical models are proposed to determine the two critical velocities for the transition from particle aggregation to separation and obtain a critical radius below which the colliding particles always aggregate. Molecular simulation results with coarse grain potentials agreed well with the analytical predictions for the critical radius for a group of model materials.

In this section, we further studied the head-on collision in two kinds of particles with real materials, i.e., tungsten and copper. The material properties, including the γ_{us} and γ_s, are obtained from the literature for the tungsten [42] and the copper [43] and are listed in Table 2. In the following analysis, we evaluated the critical radius by Eq. (6) with R_0 being $\sim 5.87b$.

The collision model for tungsten and copper particles is similar to the model illustrated in Fig. 1. In the simulations, the atoms in the tungsten particles are constructed in a body-centered cubic (BCC) single crystalline structure with crystal orientations being x-[100], y-[010], and z-[001], respectively. The atoms in copper particles are located in FCC single crystalline structure with orientations being x-[100], y-[010], and z-[001], respectively. The embedded atom method (EAM) potentials are used to describe the interactions among tungsten atoms [42] and copper atoms [43]. The radius of particles is 10 nm, and the temperature is 300 K. The initial velocity of the particle ranges from 20 m/s to 700 m/s.

4.1. Collision of tungsten particles

For tungsten, the critical radius for aggregation is evaluated as ~ 3 nm by the analytical model, and thus the particles with a radius of 10 nm would separate at a specific range of impact velocities. As expected, Fig. 9(a) shows there exist two critical velocities for the transition of particle aggregation and separation. The tungsten particles separate at the impact velocities ranging from 150 m/s to 600 m/s. Similar to the results in Fig. 2, there exists a peak restitution coefficient at the impact velocity of ~ 250 m/s because of the cohesive interaction and the repulsive interaction between particles [33]. The colliding deformation can be further understood by analyzing the atomic equivalent strain [44]. As shown in Fig. 9(b), at the impact velocity of 300 m/s, the particle deformation is mainly concentrated at the edge of the contact area during the collision, featuring a high value of atomic equivalent strain. In contrast, at the impact velocity of 700 m/s, the plastic deformation widely exists in the contact zone, resulting in a full yielding of the particles. As a result, the particles aggregate after the collision.

4.2. Collision of copper particles

For copper, the value of γ_s/γ_{us} is as high as ~ 8.5, and the critical radius determined by the analytical model is ~ 13 nm. Therefore, as shown in Fig. 10, the particles with a radius of 10 nm can always aggregate after the collision at impact velocities ranging from 20 m/s to 300 m/s, and we also confirmed the aggregation of particles with the impact velocity increasing to 700 m/s. The colliding deformation of copper particles is studied by analyzing the dislocations (see Fig. 10). For impact velocity as low as ~ 20 m/s, the particle deformation is elastic, featuring no dislocations during the collision. As the impact velocity increases to ~ 100 m/s, dislocations nucleate at the contact zone, and plastic deformation involves. Furthermore, for particle collision with a high impact velocity exceeding ~ 150 m/s, dislocations nucleate and multiply throughout the whole particles, and the two particles aggregate after the collision due to the massive dislocation plasticity.

5. Summary and conclusions

In this work, we clarified when and how the particles aggregate or separate during head-on collisions. Analytical models were proposed to determine the critical impact velocities for the transition of particle collisions from aggregation to separation, and the analytical results are confirmed by the MD simulations of collisions using a group of model materials and two metal materials. The main conclusions are summarized as follows:

1) For head-on collisions of particles, two critical velocities are revealed for the transition from particle separation to aggregation. Both analytical models and simulation results indicated that the two critical velocities exhibit an opposite dependence on the particle size. As the particle size becomes larger, the low critical velocity decreases but the high one increases.

2) The particle aggregation at low and high impact velocities can be attributed to different impact mechanisms. At the low velocity, the adhesion dominates particle aggregation and suppresses the repulsion by elastic rebound. In contrast, for high velocity impact, the plasticity dominates the aggregation and dissipates the kinetic energy with little elastic recovery; in this case, the dislocation density exhibits a linear dependence on the impact velocity.

3) Combining the two critical velocities, we proposed a critical particle size below which the particles would always aggregate after a collision. The critical size for particle aggregation depends on material properties such as surface energy γ_s and unstable stacking fault energy γ_{us}. Both analytical models and simulation results demonstrated that the critical size has a linear relation with the γ_s / γ_{us}.

Data Availability Statement

The data that support the findings of this study are available from the corresponding author upon reasonable request.

Ethical approval

This article does not contain any studies with human participants or animals performed by any of the authors.

CRediT authorship contribution statement

Jianqiao Hu: Conceptualization, Validation, Methodology, Investigation, Formal analysis, Writing – original draft, Data curation, Project administration, Funding acquisition. **Xiaoming Liu:** Project administration, Conceptualization, Writing – review & editing, Supervision, Funding acquisition. **Yueguang Wei:** Supervision, Resources.

Declaration of Competing Interest

The authors declare that they have no known competing financial interests or personal relationships that could have appeared to influence the work reported in this paper.

Acknowledgement

Supplementary materials

Supplementary material associated with this article can be found, in the online version, at doi: 10.1016/j.ijimpeng.2022.104388

Appendix A. Coarse-grained interatomic potentials and flattened hardness

The coarse-grained interatomic potentials are introduced in this appendix. Following the potential in [29], the material ductility can be modified by changing the tail of a Morse potential, and the modified Morse potentials are expressed as follows:

$$\frac{E(r)}{\varepsilon_0} = \begin{cases} e^{-2\alpha_0(r-r_0)} - 2e^{-\alpha_0(r-r_0)} & r < 1.1r_0 \\ a_3 r^3 + a_2 r^2 + a_1 r^1 + a_0 & 1.1r_0 \leq r < r_c \\ 0 & r_c \leq r \end{cases} \tag{7}$$

Here, $E(r)$ is the potential energy between two atoms with distance r. ε_0 is the depth of the potential well and is set to 1.0, and r_0 is the equilibrium bond distance. α_0 governs the bond stiffness and is equal to $7.3r_0^{-1}$. The truncation at $1.1r_0$ ensures the elastic properties unchanged up to 10% strain. The r_c is a parameter that governs the tail of interatomic potentials. The parameters $a_0 \sim a_3$ ensure the continuity of the bond energy and the force.

In this study, three sets of potentials are constructed, as shown in Table A1 and Fig. A1(a). The surface energy is the same for all potentials, whereas the unstable stacking fault energy decreases as the cut-off radius increases. Generally, the potential with a shorter cut-off radius ($r_c = 1.22r_0$) corresponds to a more brittle material. In contrast, the increase in cut-off radius (e.g., $r_c = 1.38r_0$) makes the material more ductile. Therefore, based on these three model materials characterized by the modified potentials, we essentially studied the collision of particles of different ductility. Furthermore, to modify the surface energy between particles, we replaced the potential well ε_0 by $\lambda \cdot \varepsilon_0$ with λ being an adhesion ratio. By this method, we changed the surface energy γ_s to $\lambda \cdot \gamma_s$.

All the simulation models with the modified Morse potentials are constructed in the FCC structure with the lattice constant a being $\sqrt{2}r_0$. The Young's modulus for all materials is $150\varepsilon r_0^{-3}$ [45]. To obtain the particle hardness, we performed the flattening of a hemispherical particle on a substrate, see the inset in Fig. A1(b). The flattening is carried out at the temperature of $0.005\varepsilon/k_B$ and the velocity of $0.05r_0/t_0$, and the results are shown in Table A1 and Fig. A1(b). The flattening hardness is calculated by averaging the contact stresses at the normalized depth S_z/R between 0.3 and 0.5, and the standard deviation is calculated to present the error bar of hardness. It can be seen that the particle with more brittle material has a larger hardness.

Table A 1
Materials with modified Morse potentials and the hardness.

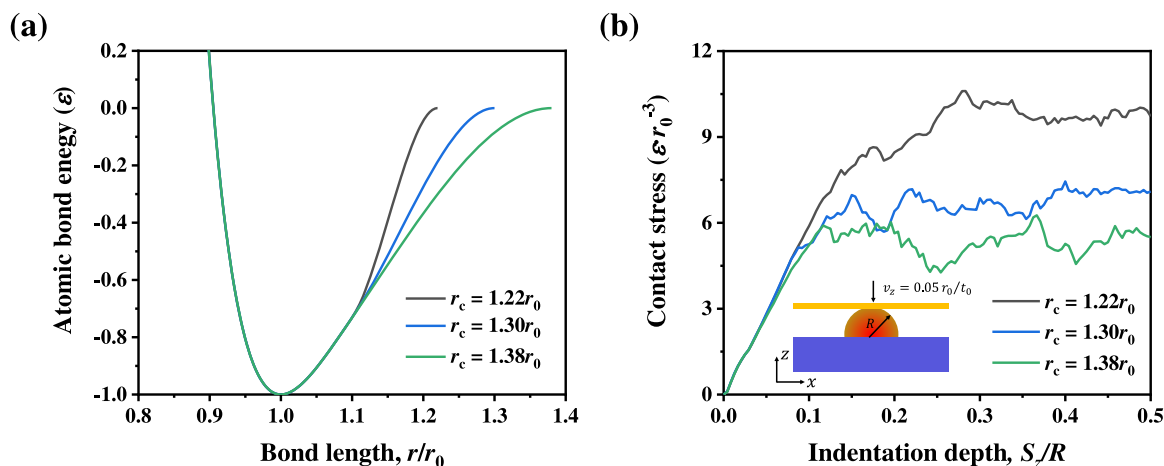| Cut-off radius, $r_c (r_0)$	Flattening hardness, Y (εr_0^{-3})	Unstable stacking fault energy, γ_{us} (εr_0^{-2})	Surface energy on (001) Plane, γ_s (εr_0^{-2})
1.22	9.8±0.2	1.248	2.000
1.30	6.9±0.3	0.722	2.000
1.38	5.4±0.3	0.534	2.000

(a)

(b)

Fig. A1. (a) The bond energy versus atomic bond length for different cut-off radius r_c. (b) Contact stress for materials with potentials of different r_c; the inset illustrates the flattening model with a hemispherical particle of radius $30r_0$.

References

[1] Zhao W, Lv Y, Zhou Q, Yan W. Investigation on particle deposition criterion and dust accumulation impact on solar PV module performance. Energy 2021;233: 121240.

[2] Zhao W, Lv Y, Zhou Q, Yan W. Collision-adhesion mechanism of particles and dust deposition simulation on solar PV modules. Renew Energy 2021;176:169–82.

[3] Karthikeyan J. The advantages and disadvantages of the cold spray coating process. Cold Spray Mater Depos Process 2007:62–71.

[4] Hou Z, Li J, Zhou Z, Pei Y. Programmable particles patterning by multifrequency excitation radiation force of acoustic resonance modes. Int J Mech Sci 2022;222: 107232.

[5] Brilliantov NV, Albers N, Spahn F, Poschel T. Collision dynamics of granular particles with adhesion. Phys. Rev. E, Stat. Nonlinear Soft Matter Phys. 2007;76(5): 051302.

[6] Hou Z, Zhou Z, Lv Z, Pei Y. Particles separation using the inverse Chladni pattern enhanced local Brazil nut effect. Extreme Mech. Lett. 2021;49:101466.

[7] Kuninaka H, Hayakawa H. Anomalous behavior of the coefficient of normal restitution in oblique impact. Phys Rev Lett 2004;93(15):154301.

[8] Lu Y, Huang F, Liu X, Ao X. On the failure pattern of sandstone impacted by high-velocity water jet. Int J Impact Eng 2015;76:67–74.

[9] Wu D, Zhou P, Wang G, Howes T, Chen W. A theoretical study of particle coalescence criteria for inelastic collisions of wet particles. Chem Eng Sci 2021; 243:116770.

[10] Roisman IV. Hydrodynamic model of a collision of a spherical plastic ice particle with a perfectly rigid substrate. Int J Impact Eng 2021:104019.

[11] Mueller P, Antonyuk S, Stasiak M, Tomas J, Heinrich S. The normal and oblique impact of three types of wet granules. Granular Matter 2011;13(4):455–63.

[12] Ye Y, Zeng Y. A size-dependent viscoelastic normal contact model for particle collision. Int J Impact Eng 2017;106:120–32.

[13] Wu C, Li L, Thornton C. Energy dissipation during normal impact of elastic and elastic–plastic spheres. Int J Impact Eng 2005;32(1-4):593–604.

[14] Han LB, An Q, Luo SN, Goddard WA. Ultra-elastic and inelastic impact of Cu nanoparticles. Mater Lett 2010;64(20):2230–2.

[15] Hu J, Song H, Liu Z, Zhuang Z, Liu X, Sandfeld S. Predicting the flow stress and dominant yielding mechanisms: analytical models based on discrete dislocation plasticity. Sci Rep 2019;9(1):20422.

[16] Phung-Van P, Thai CH, Nguyen-Xuan H, Abdel-Wahab M. An isogeometric approach of static and free vibration analyses for porous FG nanoplates. Eur J Mech A Solids 2019;78:103851.

[17] Germann TC. Large-scale molecular dynamics simulations of hyperthermal cluster impact. Int J Impact Eng 2006;33(1-12):285–93.

[18] Suri M, Dumitrică T. Efficient sticking of surface-passivated Si nanospheres via phase-transition plasticity. Phys Rev B 2008;78(8):081405.

[19] Tomas J. Adhesion of ultrafine particles—A micromechanical approach. Chem Eng Sci 2007;62(7):1997–2010.

[20] Thornton C, Ning Z. A theoretical model for the stick/bounce behaviour of adhesive, elastic-plastic spheres. Powder Technol 1998;99(2):154–62.

[21] Weir G, McGavin P. The coefficient of restitution for the idealized impact of a spherical, nano-scale particle on a rigid plane. Proc R Soc A Math Phys Eng Sci 2008;464(2093):1295–307.

[22] Millan EN, Tramontina DR, Urbassek HM, Bringa EM. The elastic-plastic transition in nanoparticle collisions. Phys Chem Chem Phys 2016;18:3423–9.

[23] Millan EN, Tramontina DR, Urbassek HM, Bringa EM. Nucleation of plasticity in nanoparticle collisions. Phys Rev E Stat Nonlinear Soft Matter Phys 2016;93(6): 063004.

[24] Kalweit M, Drikakis D. Collision dynamics of nanoscale Lennard-Jones clusters. Phys Rev B 2006;74(23):235415.

[25] Takato Y, Sen S, Lechman JB. Strong plastic deformation and softening of fast colliding nanoparticles. Phys Rev E Stat Nonlinear Soft Matter Phys 2014;89(3): 033308.

[26] Jung S, Bang J, Yoon W. Applicability of the macro-scale elastic contact theories for the prediction of nano-scaled particle collision with a rigid flat surface under non-adhesive and weakly-adhesive conditions. J Aerosol Sci 2012;50:26–37.

[27] Higa M, Arakawa M, Maeno N. Size dependence of restitution coefficients of ice in relation to collision strength. Icarus 1998;133:310–20.

[28] Ohnishi N, Bringa EM, Remington BA, Gilmer G, Minich R, Yamaguchi Y, Tielens AGGM. Numerical analysis of nanograin collision by classical molecular dynamics. J Phys Conf Ser 2008;112(4):042017.

[29] Aghababaei R, Warner DH, Molinari JF. Critical length scale controls adhesive wear mechanisms. Nat Commun 2016;7:11816.

[30] Plimpton S. Fast parallel algorithms for short-range molecular dynamics. J Comput Phys 1995;117(1):1–19.

[31] Stukowski A, Albe K. Extracting dislocations and non-dislocation crystal defects from atomistic simulation data. Modell Simul Mater Sci Eng 2010;18(8):085001.

[32] Stukowski A. Visualization and analysis of atomistic simulation data with OVITO–the open visualization tool. Modell Simul Mater Sci Eng 2010;18(1): 015012.

[33] Kuninaka H, Hayakawa H. Simulation of cohesive head-on collisions of thermally activated nanoclusters. Phys Rev E Stat Nonlinear Soft Matter Phys 2009;79(3): 031309.

[34] Sun Y, Veysset D, Nelson KA, Schuh CA. In situ observations of jetting in the divergent rebound regime for high-velocity metallic microparticle impact. Appl Phys Lett 2020;117(13):134105.

[35] Rennecke S, Weber AP. The critical velocity for nanoparticle rebound measured in a low pressure impactor. J Aerosol Sci 2013;58:135–47.

[36] R.Rice J. Dislocation nucleation from a crack tip: An analysis based on the Peierls concept. J Mech Phys Solids 1992;40(2):239–71.

[37] Sun Y, Veysset D, Nelson KA, Schuh CA. The transition from rebound to bonding in high-velocity metallic microparticle impacts: jetting-associated power-law divergence. J Appl Mech 2020;87(9):091002.

[38] Tiamiyu AA, Sun Y, Nelson KA, Schuh CA. Site-specific study of jetting, bonding, and local deformation during high-velocity metallic microparticle impact. Acta Mater 2021;202:159–69.

[39] Kelchner CL, Plimpton SJ, Hamilton JC. Dislocation nucleation and defect structure during surface indentation. Phys Rev B 1998;58(17):11085–8.

[40] Antonyuk S, Heinrich S, Tomas J, Deen NG, van Buijtenen MS, Kuipers JAM. Energy absorption during compression and impact of dry elastic-plastic spherical granules. Granular Matter 2010;12(1):15–47.

[41] Murakami R, Hayakawa H. Effect of elastic vibrations on normal head-on collisions of isothermal spheres. Phys Rev E Stat Nonlinear Soft Matter Phys 2014;89(1): 012205.

[42] Marinica MC, Ventelon L, Gilbert MR, Proville L, Dudarev SL, Marian J, Bencteux G, Willaime F. Interatomic potentials for modelling radiation defects and dislocations in tungsten. J Phys Condens Matter 2013;25(39):395502.

[43] Mishin Y, Mehl MJ, Papaconstantopoulos DA, Voter AF, Kress JD. Structural stability and lattice defects in copper:Ab initio, tight-binding, and embedded-atom calculations. Phys Rev B 2001;63(22):224106.

[44] Shimizu F, Ogata S, Li J. Theory of shear banding in metallic glasses and molecular dynamics calculations. Mater Trans 2007;48(11):2923–7.

[45] Aghababaei R. On the origins of third-body particle formation during adhesive wear. Wear 2019;426–7. 1076-1081.